1   **Observations of iodine monoxide over three summers at the Indian Antarctic bases, Bharati**

2   **and Maitri**

3   Anoop S. Mahajan[1*], Mriganka S. Biswas[1,2], Steffen Beirle[3], Thomas Wagner[3], Anja Schönhardt[4],

4   Nuria Benavent[5] and Alfonso Saiz-Lopez[5]

5   [1]Centre for Climate Change Research, Indian Institute of Tropical Meteorology, Ministry of Earth

6   Sciences, Pune, 411008 India.

7   [2]Savitribai Phule Pune University, Pune, 411008 India.

8   [3]Max-Planck-Institut für Chemie (MPI-C), Satellitenfernerkundung, 55128 Mainz, Germany

9   [4]Institute of Environmental Physics, Department of Physics and Electrical Engineering, University

10   of Bremen, Bremen, 330440 Germany.

11   [5]Department of Atmospheric Chemistry and Climate, Institute of Physical Chemistry Rocasolano,

12   CSIC, Madrid 28006, Spain

13

14   * corresponding author: Anoop S. Mahajan (anoop@tropmet.res.in)

15

16   **Abstract**

17   Iodine plays a vital role in oxidation chemistry over Antarctica, with past observations showing

18   highly elevated levels of iodine oxide (IO) leading to severe depletion of boundary layer ozone in

19   West Antarctica. Here, we present multi axis differential absorption spectroscopy (MAX-DOAS)

20   based observations of IO over three summers (2015-2017) at the Indian Antarctic bases, Bharati

21   and Maitri. IO was observed during all the campaigns, with mixing ratios below 2 pptv for the

22   three summers, which are lower than the peak levels observed in West Antarctica. This suggests

23   that sources in West Antarctica are different or stronger than sources of iodine compounds in East

24   Antarctica. Vertical profiles estimated using a profile retrieval algorithm showed decreasing

25   gradients, with a peak in the lower boundary layer. The ground-based instrument retrieved vertical

26   column densities (VCDs) were approximately a factor of three-five higher than the VCDs reported

27   using satellite-based instruments, which is most likely related to the sensitivies of the

28   measurement techniques. Airmass back-trajectory analysis failed to highlight a source region, with

29   most of the airmasses coming from coastal or continental regions. This study highlights the

30   variation in iodine chemistry in different regions in Antarctica and the importance of a long-term

31   dataset to validate models estimating the impacts of iodine chemistry.

32

33   Keywords: Iodine; Antarctica; halogens; DOAS

34   **1. Introduction**

35   Observations of reactive halogen species (RHS) have been made in the Antarctic marine boundary

36   layer (MBL) for almost two decades. Early observations focused on bromine oxide (BrO), the

37   presence of which was observed in the Antarctic using ground based instruments (Kreher et al.,

38   1997) and via satellites (Hollwedel et al., 2004). The presence of iodine oxide (IO) in the Antarctic

39   atmosphere was also confirmed through integrated column measurements from the ground (Frieß

40   et al., 2001). Later, long term ground-based observations of RHS made at Halley Bay showed the

41   critical role that bromine and iodine compounds play in regulating the oxidizing capacity, causing

42   ozone depletion and new particle formation in the Antarctic MBL. These ground-based

43   observations showed that both IO and BrO, are present at elevated concentrations in certain parts

44   of the Antarctic MBL, and show a significant seasonal variation peaking in the spring, with

45   elevated concentrations observed through the summer (Saiz-Lopez et al., 2007a, 2008). Satellite-

46   based observations of both IO and BrO reported a similar annual cycle, although with large

47   geographical differences (Hollwedel et al., 2004; Richter et al., 2002; Saiz-Lopez et al., 2007b;

48   Schönhardt et al., 2008, 2012; Theys et al., 2011; Wagner et al., 2001). These satellite observations

49   have been validated by ground-based observations, although most of them have hitherto focused

50   around the Weddell Sea (Atkinson et al., 2012; Buys et al., 2013; Frieß et al., 2001, 2010; Saiz-

51   Lopez et al., 2007a, 2008). Ground-based observations have also been made at McMurdo Sound,

52   near the Ross Sea, where lower concentrations of IO were observed (Hay, 2010). Additional

53   observations over the 2011-2012 summer were made at Dumont d'Urville using a cavity enhanced

54   absorption spectroscopy based instrument and showed a maximum of 0.15 pptv of IO (Grilli et al.,

55   2013). However, to date observations of IO have not been reported in the Indian Ocean sector of

56   the Antarctic peninsula (Saiz-Lopez et al., 2012; Saiz-Lopez and von Glasow, 2012).

57   Ground based observations at Halley Bay and in the Weddell Sea suggest that the main source of

58   iodine compounds is the sea ice region (Atkinson et al., 2012; Saiz-Lopez et al., 2007a). The exact

59   process is still not known, although a mechanism for biologically-induced iodine emissions from

60   sea-ice has been suggested based on the idea that micro-algae are the primary source of iodine

61   emissions in this environment (Saiz-Lopez et al., 2015a). There are further questions regarding the

62   propagation of reactive iodine chemistry across the continent because satellite observations show

63   the presence of IO deep within the Antarctic continent, even as far as the South Pole (Saiz-Lopez

64   et al., 2007b; Schönhardt et al., 2008). However, although enhanced, the observed IO column

65   densities are close to the detection limit of the satellite instrument and are therefore subject to

66   uncertainties. One study by Frieß et al. (2010) suggested a strong source within the snowpack,

67   which hints at active recycling and re-emission of IO aiding the long transport inland. However,

68   questions remain about why such a source would function only in parts of the continent and why

69   the primary source is different from the Arctic, where much lower peak concentrations are

70   sporadically observed (Mahajan et al., 2010; Saiz-Lopez and Blaszczak-boxe, 2016). To further

71   understand the sources of iodine in the polar environment, understanding the geographical

72   distribution is critical. Satellite observations play a useful role for this, although validation of the

73   satellite observations using ground-based instruments is necessary to ascertain their accuracy to

74   observe IO in the Antarctic troposphere.

75   Questions also remain about the vertical profiles of iodine compounds in the Antarctic boundary

76   layer and above the boundary layer. Modelling based studies have suggested a strong gradient

77   from the surface to the edge of the boundary layer (Saiz-Lopez et al., 2008). Only once in the past

78   have vertical profiles of IO been measured in Antarctica. These measurements were made at

79   McMurdo Sound in East Antarctica (Hay, 2010). Observations over two "golden days" in 2006

80   and 2007 show surface concentrations of about 1 pptv, decreasing to ~0.2 pptv at about 200 m,

81   before reaching a second maximum of 0.6 pptv at ~700 m. However, models did not reproduce

82   this profile shape and the authors did mention that the observations had large uncertainties with

83   the a priori providing most of the information for the profile retrieval (Hay, 2010). In most models,

84   the assumption is that the source is from the snowpack, with photochemistry in the atmosphere

85   resulting in a steady decrease with altitude. However, considerable challenges remain in

86   reproducing the surface variation and vertical gradients in addition to the geographical distribution

87   (Fernandez et al., 2019). More recent modelling studies combined with aircraft observations

88   suggest that the gradient is not very sharp all over the globe, with a significant free tropospheric

89   and stratospheric contribution to the total column (Koenig et al., 2020; Saiz-Lopez et al., 2015b),

90   although such observations have still not been done in the Antarctic. One of the main reasons for

91   the uncertainties in models is the lack of consistent measurements of vertical gradients across the

92   world, especially in the Polar Regions like Antarctica to validate these model simulations.

93   Considering the uncertainties in the satellite observations and questions regarding the sources and

94   vertical and geographical distribution of IO, further observations are necessary. Here we present

95   observations made at two new locations in Antarctica over three summers and compare them with

96   the satellite-based retrievals and past observations.

97

98   **2. Methodology**

99   Figure 1 shows the location of the two Indian Antarctic stations, Maitri (11.73 °E , 70.77 °S) and

100   Bharati (76.19 °E, 69.41 °S). The other stations where observations of IO have been reported in

101   the past are also marked on the map. Observations of IO and the oxygen dimer (O_4) were made

Atmospheric
Chemistry
and Physics
Discussions

Open Access

EGU

102   using the Multi-Axis Differential Optical Absorption Spectroscopy technique (MAX-DOAS) over

103   three summers: February-March 2015 as a part of the 34th Indian Scientific Expedition to

104   Antarctica (ISEA-34), November 2015 – February 2016 as a part of ISEA-35 and January-

105   February 2017 as a part of ISEA-36.

106   Observations at the Maitri station were made over a short span of 9 days (9th March – 17th March

107   2015) and only during ISEA-34. The research station is in the ice-free rocky area on the

108   Schirmacher Oasis. The MAX-DOAS instrument was installed in a summer-time residential

109   container, ~150 m north the station, about 120 m above sea level during the ISEA-34. The scanner

110   unit was mounted on top of the container with the clear line of sight to the horizon. The scanner

111   pointed ~60.0° with respect to magnetic north. The spectrometer unit was kept inside the container,

112   which was temperature controlled. The open ocean is 125 km north of Maitri.

113   Observations at the Bharati station were made for 10 days (9th February-18th February 2015) during

114   ISEA-34, for 63 days (30th November 2015 – 1st February 2016) during ISEA-35 and for 35 days

115   (5th January-11th February 2017) during ISEA-36. The station is located between the Thala Fjord

116   and Quilty Bay, east of the Stornes Peninsula. The MAX-DOAS instrument was installed in a hut

117   on top of a ridge around 200 m south-west of the Bharati station and was approximately 56 m

118   above sea level. The scanner unit was mounted on the wall of the hut and had a clear line of sight

119   to the horizon, pointing -23.2° with respect to the north, overlooking the open ocean. The coastline

120   is within 500 m of the hut, but it becomes ice free from mid-January to late March. Depending on

121   the sea ice conditions, the open ocean is within 8-10 km north from the end of November.

122   The MAX-DOAS instrument (EnviMes) makes use of scattered sunlight along different elevation

123   angles and by combination of several lines of sight including the zenith. The concentration of an

Atmospheric
Chemistry
and Physics
Discussions
Open Access
EGU

124   absorber in the boundary layer can be obtained either in a first approximation by a simple

125   geometric approach or by simulating the light path with a radiative transfer model taking into

126   account also multiple scattering effects and the correct treatment of the aerosol loading in the

127   atmosphere (Hönninger et al., 2004; Platt and Stutz, 2008; Wagner et al., 2004). The instrument

128   consists of an indoor unit, housing a spectrometer with a spectral resolution of 0.7 nm (UV: 301.20-

129   463.69), which is connected to an outdoor unit, containing a scanning telescope. Discrete elevation

130   angles (1°, 2°, 3°, 5°, 7°, 10°, 20°, 40°, and 90°) were recorded for a total exposure time of 1

131   minute each during all the three campaigns. The spectra were recalibrated before analysis using

132   mercury emission lines recorded at the end of each day. For DOAS retrieval, the QDOAS 3.2

133   software was used (Fayt and Van Roozendael, 2013). For estimation of the O_4 Differential Slant

134   Column Densities (DSCDs), the cross-sections of O_4 (Thalman and Volkamer, 2013) at 293K;

135   NO_2 (Vandaele et al., 1998) at 294 K and 220 K (orthogonalized to NO_2 at 294 K); O_3 (Bogumil

136   et al., 2003) at 223 K and 243 K (orthogonalized to O_3 at 243 K); HCHO (Meller and Moortgat,

137   2000) at 298 K; HONO (Stutz et al., 2000) at 296 K were used in the 351-390 nm window. The

138   cross-sections used for IO retrieval in the 417-440 nm spectral window were: IO (Gómez Martín

139   et al., 2005), NO_2 220 K and 298 K (Vandaele et al., 1997), H_2O (Rothman et al., 2013), O_4

140   (Thalman and Volkamer, 2013) and O_3 (Bogumil et al., 2003). In addition to these cross-sections

141   a ring spectrum (Chance and Spurr, 1997), a second ring spectrum following Wagner et al. (2009),

142   and the 3rd order polynomial were used for both windows. The zenith spectrum from each scan

143   was used as a reference to remove contribution from possible free tropospheric or stratospheric

144   absorption. An example of a DOAS fit for O_4 and IO are given in Figure S1. Surface mixing ratios

145   and the total vertical column densities (VCDs) were retrieved from the MAX-DOAS DSCDs of

146   IO and O_4 by employing the Mainz Profile Algorithm (MAPA) (Beirle et al., 2018). Only

147   observations with solar zenith angles (SZA) less than 75° were used for the profile retrievals due

148   to the large path lengths through the stratosphere for high SZA angles. This algorithm uses a two-

149   step approach to determine the trace gas vertical profiles. In the first step, the aerosol profiles are

150   retrieved using the measured O_4 DSCDs. A Monte Carlo approach is utilized to identify the best

151   ensemble of the forward model parameters (column parameters (c) (VCD for trace gases and

152   aerosol optical depth for aerosol), height parameter (h) and shape parameter (s)), which fit the

153   measured O_4 DSCDs for the sequence of elevation angles. In the second step, the aerosol profiles

154   retrieved from the O_4 inversion are used as an input to retrieve similar model parameters (c, h, and

155   s) for IO. The state of the atmosphere was calculated using the pressure and temperature profiles

156   observed by the in situ radiosondes, which were launched once a week at both the stations. An

157   angstrom exponent of 1 was used for the difference in the retrieval wavelengths as per observations

158   made at Bharati in the past (Prakash Chaubey et al., 2011). Within MAPA, the differential air mass

159   factors (AMFs) are calculated offline with the radiative transfer model McArtim (Deutschmann et

160   al., 2011) for fixed nodes for each parameter and stored as a lookup table (LUT) for quick analysis.

161   To assess the quality of the retrievals, MAPA also provides "valid", "warning" or "error" flags for

162   each measurement sequence, which are calculated based on pre-defined thresholds for various fit

163   parameters. For further details about MAPA, please refer to the description paper by Beirle et al.

164   (2018). Additionally, MAPA also provides the option to use a scaling factor for significant

165   mismatch between the modelled and measured O_4 DSCDs, which has been shown to be close to

166   0.8 in the past (Wagner et al., 2019). Using the variable option, where the model estimates the

167   scaling factor, the estimated value of which ranged between 0.75 and 0.9. Hence a scaling factor

168   of 0.8 was applied for all the campaigns.

169   We also make use of the IO vertical column densities retrieved using the SCanning Imaging

170   Absorption spectroMeter for Atmospheric CHartographY (SCIAMACHY), a UV-vis-NIR

171   spectrometer onboard the ENVISAT satellite (Burrows et al., 1995). Observations from

172   SCIAMACHY stopped due to instrumental problems in April 2012. Here we make use of the mean

173   from 2004-2011 to look at the geographical distribution and compare it with the ground-based

174   observations made during this study. Further details about the IO retrieval algorithm and the

175   SCIAMACHY instrumental setup can be found elsewhere (Schönhardt et al., 2008, 2012).

176

177   **3. Results and Discussion**

178   **3.1 Meteorological parameters**

179   Figure 2 shows the 5-day back-trajectories arriving every hour at the two stations at a height of 10

180   m on the days that the DOAS measurements were conducted as a part of the three ISEA

181   expeditions. The back-trajectories were calculated using the HYbrid Single-Particle Lagrangian

182   Integrated Trajectory (HYSPLIT) using the using the EDAS-40 km database (Draxler and Rolph,

183   2003). The trajectories show that the airmasses sampled throughout the three expeditions were

184   from either a remote oceanic region, coastal Antarctica, or the continental shelf. In general, most

185   of the trajectories show that the airmasses had travelled over hundreds of kilometres over the last

186   five days. For the local meteorological conditions, Figure 3 (top panels) show the wind direction

187   at the Bharati station. Most of the time, the wind was from the ocean, with the winds coming from

188   the north-west sector and a few instances of northern and north eastern winds. This was during all

189   the three expeditions at the Bharati station. The wind speed was mostly below 20 knots (~10 m s^{-}

190   ^{1}) for all the campaigns, although periods of high winds were observed during ISEA-35 and ISEA-

191   36, which were of a longer duration than ISEA-34. The temperature at the station hovered between

192   -5°C and +5°C, through the summer period, with higher values closer to noon (Figure 3, middle

193   panels). The humidity fluctuated from 40% to above 90%. The radiation followed a clear diurnal

194   pattern, with the highest values seen around local noon and minima at local midnight. Considering

195   that this region sees light for 24 hours, the radiation also showed a non-zero minima between

196   November to January (Figure 3, bottom panels). However, in February, a clear night-time is seen

197   in the radiation data. Finally, a measure of the cloudiness was also tracked using visual full sky

198   cloud cover observations. Any cloud cover of more than 30% was considered to be cloudy (cloud

199   flag value of 1), which helps in filtering the MAX-DOAS observations. In addition to the visual

200   inspection of the sky, which was performed once an hour, a second cloud index was calculated

201   based on the ratios of the radiances at 320 nm and 440 nm from the 3° and zenith spectra (Mahajan

202   et al., 2012; Wagner et al., 2014). Both the manual and radiance-based indices showed a close

203   match, indicating that cloudy conditions were well discerned by the cloud index calculation.

204   Meteorological data was unfortunately not available at the Maitri station.

205   **3.2 Differential Slant Column Densities (DSCDs)**

206   Figure 4 shows the observed O_4 DSCDs at different elevation angles for all the campaigns. O_4

207   DSCDs were found to be higher at lower elevation angles, as expected, which is because the O_4

208   concentration is proportional to the square of the oxygen pressure and thus increases towards the

209   surface. This also suggests that the aerosol loading was low in the atmosphere. Photons travel

210   longer paths at lower elevation angles and interact more with tropospheric absorbing species before

211   reaching the instrument resulting in a decreasing profile with increasing elevation angles. The

212   average residual root mean square (RMS) and 2σ detection limit for the O_4 DSCDs were $4.46 \times 10^{-}$

213   ^{4} (range: $1.56\text{-}10.01 \times 10^{-4}$) and 2.11×10^{42} molecules^2 cm^{-5} (range: $0.72\text{-}4.66 \times 10^{42}$ molecules^2

214   cm$^{-5)}$, respectively (Figure 4). The O$_4$ DSCDs were then used to estimate the aerosol profiles and

215   hence the IO mixing ratios, as described earlier in section 2.

216   Figure 5 shows the observed IO DSCDs at different elevation angles for all the campaigns. The

217   IO DSCDs were found to be higher at lower elevation angles, which indicates a decreasing gradient

218   in the IO vertical profile. The residual RMS was in the 1.15-9.73×10^{-4} range (mean: 3.46×10^{-4}),

219   resulting in 2σ IO DSCD detection limits of 6.57×10^{12} to 5.71×10^{13} molecules cm^{-2} (mean

220   1.88×10^{13} molecules cm^{-2}) (Figure 5). For several days, only the lowermost elevation angles were

221   found to be above the two-sigma detection limit of the instrument. Higher IO DSCDs were

222   observed at high SZAs, which is related to an increase in the path length. However, only

223   observations with SZA<75° were used to estimate the vertical profiles and surface mixing ratios

224   using the aerosol profiles derived using the O$_4$ DSCDs, as described earlier in section 2. A zoomed

225   in view of two days for both the O$_4$ and IO DSCDs is shown in Figure S2, which clearly shows

226   the decreasing gradient with increasing elevation angles.

227   **3.3 IO Vertical Column Densities (VCDs) and mixing ratio profiles**

228   The O$_4$ and IO DSCDs were used to retrieve the vertical column densities and the vertical profiles

229   for aerosols and IO. A comparison of the MAX-DOAS observed O$_4$ DSCDs with the MAPA

230   modelled DSCDs for all the four campaigns are shown in Figure S3, while Figure S4 shows a

231   similar plot for the IO DSCDs. Figure 6 and 7 show the MAPA calculated AODs and IO VCDs

232   for all the campaigns. Several datapoints are flagged as error or warnings, with a few scans giving

233   a 'valid' flag. In the case of aerosols, the warning or error flags are mainly for scans which were

234   during cloudy weather (Figure S5 shows the data which were flagged as 'bad' and 'warning' along

235   with the valid scans). As mentioned above, the cloud cover was regularly measured throughout the

Atmospheric
Chemistry
and Physics
Discussions

Open Access

EGU

236   campaigns as a part of the meteorological observations. In addition to visual observations, we also

237   computed the cloud index following past works based on MAX-DOAS observations (Mahajan et

238   al., 2012; Wagner et al., 2014), which confirmed that the error and warning flags were during cloud

239   cover periods. For the valid scans, the aerosol optical depth (AOD) ranged between 0.002 and

240   0.016, with a mean value of 0.003 for ISEA-34 at Bharati; between 0.001 and 0.067, with a mean

241   value of 0.011 for ISEA-34 at Maitri; between 0.001 and 1.866, with a mean value of 0.037 for

242   ISEA-35 at Bharati; and between 0.001 and 0.878, with a mean value of 0.016 for ISEA-36 at

243   Bharati (Figure 6). The low values are expected considering the pristine conditions in Antarctica,

244   although during a couple of scans elevated levels were observed as demonstrated by the maximum

245   value during ISEA-35 and ISEA-36. In the case of IO, there were far fewer valid retrieved profiles

246   as can be seen in Figure 7 (Figure S6 shows the data which were flagged as 'bad' and 'warning'

247   along with the valid scans). One of the main reasons is that for most of the scans the IO DSCDs at

248   higher elevation angles are below the detection limit and hence not enough information is available

249   for the model to retrieve a valid vertical profile. In the case of IO VCDs, there were only two scans

250   which showed the valid flag over the 10-day period during the ISEA-34 campaign at Bharati due

251   to adverse weather conditions leading to mostly cloudy weather. Thus, the VCD value of 2.83×10^{12}

252   molecules cm^{-2}, should be treated with some caution. In Maitri during ISEA-34, the IO VCD

253   ranged between 2.37×10^{12} molecules cm^{-2} and 4.25×10^{12} molecules cm^{-2}, with a mean value of

254    $3.40 \pm 0.57 \times 10^{12}$ molecules cm^{-2}. During ISEA-35 at Bharati, which had the highest number of

255   valid scans over the four campaigns, the IO VCDs ranged between 0.01×10^{12} and 5.86×10^{12}

256   molecules cm^{-2}, with a mean value of $2.62 \pm 1.16 \times 10^{12}$ molecules cm^{-2}. During ISEA-36, the IO

257   VCDs ranged between 2.78×10^{12} molecules cm^{-2} and 4.90×10^{12} molecules cm^{-2}, with a mean value

258   of $3.92 \pm 0.79 \times 10^{12}$ molecules cm^{-2} at Bharati.

259   In addition to the VCDs, vertical profiles of aerosols (Figure S7) and IO were estimated using

260   MAPA. Figure 8 shows the typical vertical profiles of IO mixing ratios over the four expeditions.

261   The surface mixing ratios for the valid scans range between 0.2 and 1.3 pptv. The surface

262   concentrations observed at both Maitri and Bharati are lower than observations in the Weddell Sea

263   region, where summer time concentrations exceeding 6 pptv have been reported in the past

264   (Atkinson et al., 2012; Saiz-Lopez et al., 2007a), or at the Neumayer station, where long-term

265   zenith sky DOAS measurements of IO suggest mixing ratios as high as ~10 pptv during the

266   summer (Frieß et al., 2001). It should be noted that although elevated concentrations were observed

267   at Halley, the average summer concentration, measured only 4 m above the snowpack using a

268   Long-Path DOAS instrument, was about 3 pptv, approximately a factor of three higher than the

269   observations at Bharati and Maitri. Considering that the MAX-DOAS retrieved profiles are not

270   very sensitive to the lowermost few meters, this discrepancy is expected. This is because the source

271   of IO is expected to be from the surface and remote sensing estimates have suggested that high IO

272   concentrations in the order of 50 ppbv are present in the snow interstitial air (Frieß et al., 2010),

273   suggesting that snowpack is indeed the source for iodine compounds. If this is indeed the case, a

274   strong gradient would be observed considering the short lifetime of IO in the atmosphere, and

275   hence the MAX-DOAS observations would be lower than the LP-DOAS observations. The

276   observations reported in this study are also similar to measurements at McMurdo Sound, near the

277   Ross Sea, where MAX-DOAS observations reported a maximum of 2.6 ± 0.1 pptv with most of

278   the observations below 1 pptv during 2006 and 2007 (Hay, 2010). McMurdo Sound is also located

279   in the East Antarctic, which shows lower levels of IO in the satellite estimates (Schönhardt et al.,

280   2008) and in models (Fernandez et al., 2019).

281   Vertical profiles of IO have been reported only once in the past from Antarctica. These

282   measurements were made at McMurdo Sound in East Antarctica (Hay, 2010). IO over two days in

283   2006 and 2007 show typical surface concentrations of ~1 pptv (with a maximum of 2.6 pptv),

284   decreasing to ~0.2 pptv at about 200 m. A second maximum of 0.6 pptv at ~700 m was also

285   observed, but the models do not reproduce this profile shape and the observations were subject to

286   large uncertainties with the vertical profile above 200 m dominated by the a priori (Hay, 2010).

287   During the four campaigns studied here, elevated concentrations, similar to the surface, were

288   usually observed until about 400 m. Above this height, there is a decrease, with the retrievals

289   reducing to below 0.1 pptv (Figure 8). The reducing standard deviations in the profile retrieval

290   with altitude show that all the profiles which reproduce elevated IO close to the ground approach

291   zero for higher altitudes, suggesting that most of the IO is within the lower part of the troposphere.

292   However, this gradient is much more gradual than estimates predicted using the THAMO one-

293   dimensional model at Halley Bay (Saiz-Lopez et al., 2008). In most models, the assumption is that

294   the source is from the snowpack, and hence a strong decreasing gradient with altitude has been

295   predicted (Saiz-Lopez et al., 2008). The gradient of this decrease depends on the photolysis of the

296   higher oxides, and on the recycling of iodine reservoir species on aerosols, both of which have

297   uncertainties. When the gradient was estimated in 2008 (Saiz-Lopez et al., 2008), the photolysis

298   rates for the higher oxides were not available but this has recently been measured in the laboratory

299   (Lewis et al., 2020) and THAMO needs to be updated accordingly. Another important point to

300   consider is that the MAX-DOAS observation-based profile retrievals typically get only a couple

301   of points of information in the boundary layer and are hence not expected to capture this strong

302   decrease.

303   **3.4 Comparison with satellite-based estimates**

304   The satellite-based vertical column densities of IO across the Weddell Sea region, and the region

305   encompassing Bharati and Maitri are shown in Figure 9. The averaged satellite based VCD

306   observations suggest that lower levels of IO are expected at both the Indian bases as compared to

307   places where ground-based observations have been reported in the past, such as Halley Bay and

308   Neumayer. The averaged value over the eight years of observations at Bharati and Maitri are

309   between $0.6\text{-}1.4\times10^{12}$ molecules cm^{-2}. This is lower than $2.62 \pm 1.16\times10^{12}$ molecules cm^{-2}

310   observed at Bharati during ISEA-35, which was the longest dataset available in this study which

311   suggests that the ground-based instruments observe larger VCDs as compared to the satellite based

312   instruments. It should however be noted that the SCIAMACHY data is an average over all the

313   seasons, and individual daily datapoints as high as 2.1×10^{12} molecules cm^{-2} have been observed.

314   Figure 10 shows the timeseries for Bharati and Maitri with daily averages (red dots) as well as

315   monthly averages (blue triangles) for the years 2004 to 2011. Satellite measurements from within

316   500 km around the stations were included in the analysis.

317   When the whole IO column is constrained to the lower 400 m, the satellite retrieved VCDs translate

318   to a range between 0.6 – 1.3 pptv. The daily satellite VCDs tend to exceed these averaged values

319   and predict mixing ratios as high as 2 pptv. This is similar to the range observed through the three

320   campaigns reported here, although observations during the spring time, when emissions of iodine

321   species have been show to peak at Halley Bay (Saiz-Lopez et al., 2007a), were not made over these

322   three campaigns. During the spring season, values as high as 20 pptv was observed at Halley Bay,

323   a factor of ten higher than during the summer at the Indian stations. However, the satellite

324   observations do not show a large peak over the springtime over both Indian stations. Another

325   outstanding question is whether the satellites are sensitive to the lower 100-200 m, considering the

326   strong gradient in IO. Figure S8 shows the block AMFs for satellite retrievals showing the

Atmospheric
Chemistry
and Physics
Discussions

Open Access
EGU

327   significant difference between the block AMFs over Antarctica at different albedo values. Over

328   the ice-covered regions in Antarctica, the satellite is sensitive to the lower troposphere as the

329   albedo is usually 0.9 or above. Observations have shown that open water has an albedo of 0.05–

330   0.2 (Jin et al., 2004), whereas the albedo of sea ice ranges between 0.6 and 0.7 for bare ice and

331   0.8–0.9 for snow-covered ice (Perovich et al., 2002). In the case of Bharati, the Quilty Bay is not

332   ice covered during the summer and hence along the light path in Bharati, the sensitivity of the

333   satellite is much lower. Use of a higher albedo would result in an underestimation of the VCD by

334   the satellite, which is the case when compared to the ground-based instruments. At Mairti this

335   should not be the case considering that Maitri is 125 km inland from the coast, and the ice shelf is

336   less than 1 km from the station along the light path. It should be noted that the MAPA LUTs are

337   calculated for a low surface albedo (5%) and hence, at least for some of the measurements, the

338   surface albedo is probably much larger, especially at Maitri. As far as we understand, the effect of

339   the surface albedo mainly cancels out in the MAX-DOAS analysis, but it could be one possible

340   uncertainty on the retrieval results Another reason for the discrepancy between the ground based

341   and satellite retrieved VCDs could be the overpass time, which was approximately 09:00 am local

342   time. Although this should not be a large factor during the summer months due to long sunlit hours,

343   and that the numbers given above were averages through the entire campaign for the ground-based

344   observations, measurements at Halley Bay have shown a strong diurnal profile peaking at noon

345   (Saiz-Lopez et al., 2007a). Hence, it is possible that the ground-based observations, which are

346   filtered for SZA>75°, capture higher values than the satellite.

347   Finally, a point to consider is that the satellite data available from SCIAMACHY is for the period

348   of 2004-2011, whereas the MAX-DOAS observations were conducted over three summers from

349   2015. This temporal discrepancy, although small considering the long satellite dataset, could

350   contribute to the difference in the retrieved VCDs. Recent observations of iodine in ice-cores in

351   the Alpine region and over Greenland have shown an increasing trend for atmospheric iodine in

352   the northern hemisphere (Cuevas et al., 2018; Legrand et al., 2018). In the Antarctic only seasonal

353   and geographical variations in halogens in the ice have been studied and no long term dataset is

354   available (Vallelonga et al., 2017). The main cause for this increase is suggested to be an increase

355   in tropospheric ozone, which drives the emission of iodine compounds from the ocean surface

356   through heterogenous chemistry at the ocean interstitial surface (Carpenter et al., 2013). Although

357   questions regarding the strength of this inorganic source in affecting IO concentrations in the

358   Southern Ocean remain (Inamdar et al., 2020; Mahajan et al., 2019), it is possible that the

359   discrepancy between the satellite and ground based data is because of a different time period.

360   However, no increasing trend was observed in the satellite data for the period between 2004-2011

361   (Figure 10), which suggests that a factor of three increase in the VCDs is most likely due to a

362   difference in the measurement technique and sensitivities rather than a change in the emissions.

363

364   **3.5 Airmass origin dependence**

365   Year-long observations at Halley Bay in West Antarctica, which were made using the LP-DOAS

366   instrument, suggested a oceanic primary source (Saiz-Lopez et al., 2007a). This was shown

367   through the tracking of airmass back-trajectories, which displayed that elevated levels of IO were

368   present in airmasses that passed over the coastal and oceanic region compared to the airmasses

369   that had only continental exposures. However, even in airmasses that had passed only over the

370   continent for the past five days, the IO levels were still above the detection limit, which suggested

371   that even if the primary source is oceanic, a secondary source from the snow pack contributed to

372 the atmospheric IO. Indeed, subsequent studies have tried to explain the snowpack source through

373 recycling of primary emissions from the ocean (Fernandez et al., 2019) and one study has even

374 suggested a strong snowpack source based on simulated observations (Frieß et al., 2010). Although

375 the levels of IO are much lower than the peak concentrations seen at Halley Bay, we studied the

376 back-trajectories to see if the origin of airmasses lead to a difference in the observed IO levels at

377 both Bharati and Maitri. Considering the short lifetime of reactive iodine compounds in the

378 atmosphere, we calculated the exposure of each HYSPLIT calculated back-trajectory according to

379 the region it passed over the last 12 hours. Depending on where the trajectories spend the most

380 amount of time, they were classified into coastal, continental, and oceanic airmasses. The coastal

381 region was defined as a 0.5° belt along the Antarctic coastline, with regions to the north and south

382 of this belt considered to be oceanic and continental (Figure S9). Using the profiles which were

383 valid, no clear dependence on the airmass origin was observed. Indeed, most of the data points at

384 both stations corresponded to airmasses which were either coastal or continental (Figure S10) and

385 is representative of the typical wind patterns during the summer season. Thus, using this dataset,

386 it was not possible to draw any conclusions regarding the possible sources of IO in this region, and

387 a longer study is needed in the future.

388

389 **4. Conclusions**

390 This study presents observations of iodine oxide (IO) at the Indian Antarctic bases Maitri and

391 Bharati made over three summers from 2015 through 2017. IO was observed intermittently during

392 all the campaigns, with mixing ratios below 2 pptv. Using a profile retrieval algorithm, vertical

393 gradients of IO were estimated, and these showed a decreasing profile with a peak in the boundary

394   layer. The vertical columns observed using the ground-based instrument are approximately a factor

395   of three-five higher than the climatological mean observed by the satellite, which could be due to

396   a difference in the measurement techniques and sensitivities. Airmass origin analysis using back-

397   trajectories did not lead to a conclusive answer about the source regions. This study suggests that

398   a longer dataset over different seasons is necessary to answer the outstanding questions regarding

399   the sources and seasonal importance of IO in the Indian Ocean sector of Antarctica.

400

401   **5. Acknowledgements**

406   **6. Author contributions:**

407   ASM conceptualised the research plan and methodology, did the analysis and wrote the

408   manuscript. MSB did the field observations. SB, TW, NB and ASL helped with the interpretation

409   of the observations and AS provided the satellite observations and helped interpret them.

410

411   **7. References**

412   Atkinson, H. M., Huang, R.-J., Chance, R., Roscoe, H. K., Hughes, C., Davison, B., Schönhardt,

413   A., Mahajan, A. S., Saiz-Lopez, A., Hoffmann, T. and Liss, P. S.: Iodine emissions from the sea

414   ice of the Weddell Sea, Atmos. Chem. Phys., 12, 11229–11244, doi:10.5194/acp-12-11229-

Atmospheric
Chemistry
and Physics
Discussions
Open Access
EGU

415   2012, 2012.

416   Beirle, S., Dörner, S., Donner, S., Remmers, J., Wang, Y. and Wagner, T.: The Mainz Profile

417   Algorithm (MAPA), Atmos. Meas. Tech. Discuss., 1–33, doi:10.5194/amt-2018-375, 2018.

418   Bogumil, K., Orphal, J., Homann, T., Voigt, S., Spietz, P., Fleischmann, O. C., Vogel, A.,

419   Hartmann, M., Kromminga, H., Bovensmann, H., Frerick, J. and Burrows, J. P.: Measurements

420   of molecular absorption spectra with the SCIAMACHY pre-flight model: instrument

421   characterization and reference data for atmospheric remote-sensing in the 230–2380 nm region,

422   J. Photochem. Photobiol. A Chem., 157(2–3), 167–184, doi:10.1016/S1010-6030(03)00062-5,

423   2003.

424   Burrows, J. P., Hölzle, E., Goede, A. P. H., Visser, H. and Fricke, W.: SCIAMACHY – Scanning

425   Imaging Absorption Spectrometer for Atmospheric Chartography, Acta Astronaut., 35, 445–451,

426   1995.

427   Buys, Z., Brough, N., Huey, L. G., Tanner, D. J., von Glasow, R. and Jones, a. E.: High

428   temporal resolution Br2, BrCl and BrO observations in coastal Antarctica, Atmos. Chem. Phys.,

429   13, 1329–1343, doi:10.5194/acp-13-1329-2013, 2013.

430   Carpenter, L. J., MacDonald, S. M., Shaw, M. D., Kumar, R., Saunders, R. W., Parthipan, R.,

431   Wilson, J. and Plane, J. M. C.: Atmospheric iodine levels influenced by sea surface emissions of

432   inorganic iodine, Nat. Geosci., 6(2), 108–111, doi:10.1038/ngeo1687, 2013.

433   Chance, K. V and Spurr, R. J.: Ring effect studies: Rayleigh scattering, including molecular

434   parameters for rotational Raman scattering, and the Fraunhofer spectrum., Appl. Opt., 36(21),

435   5224–5230 [online] Available from: http://www.ncbi.nlm.nih.gov/pubmed/18259337, 1997.

436   Cuevas, C. A., Maffezzoli, N., Corella, J. P., Spolaor, A., Vallelonga, P., Kjær, H. A., Simonsen,

437   M., Winstrup, M., Vinther, B., Horvat, C., Fernandez, R. P., Kinnison, D., Lamarque, J.-F.,

438   Barbante, C. and Saiz-Lopez, A.: Rapid increase in atmospheric iodine levels in the North

439   Atlantic since the mid-20th century, Nat. Commun., 9(1), 1452, doi:10.1038/s41467-018-03756-

440   1, 2018.

441   Deutschmann, T., Beirle, S., Frieß, U., Grzegorski, M., Kern, C., Kritten, L., Platt, U., Prados-

442   Román, C., Pukite, J., Wagner, T., Werner, B. and Pfeilsticker, K.: The Monte Carlo atmospheric

443   radiative transfer model McArtim: Introduction and validation of Jacobians and 3D features, J.

444   Quant. Spectrosc. Radiat. Transf., 112(6), 1119–1137, doi:10.1016/j.jqsrt.2010.12.009, 2011.

445   Draxler, R. and Rolph, G.: HYSPLIT (HYbrid Single Particle Lagrangian Integrated Tra-

446   jectory). Model access via NOAA ARL Ready, [online] Available from:

447   http://www.arl.noaa.gov/ready/ hysplit4.html, 2003.

448   Fayt, C. and Van Roozendael, M.: QDOAS 1.00. Software User Manual, [online] Available

449   from: http://uv-vis.aeronomie.be/software/QDOAS/, 2013.

450   Fernandez, R. P., Carmona-Balea, A., Cuevas, C. A., Barrera, J. A., Kinnison, D. E., Lamarque,

451   J., Blaszczak-Boxe, C., Kim, K., Choi, W., Hay, T., Blechschmidt, A., Schönhardt, A., Burrows,

452   J. P. and Saiz-Lopez, A.: Modeling the Sources and Chemistry of Polar Tropospheric Halogens

453   (Cl, Br, and I) Using the CAM-Chem Global Chemistry-Climate Model, J. Adv. Model. Earth

454   Syst., 11(7), 2259–2289, doi:10.1029/2019MS001655, 2019.

455   Frieß, U., Wagner, T., Pundt, I., Pfeilsticker, K., Platt, U. and Friefi, U.: Spectroscopic

456   Measurements of Tropospheric Iodine Oxide at Neumayer Station, Antarctica, Geophys. Res.

457   Lett., 28(10), 1941–1944, 2001.

458   Frieß, U., Deutschmann, T., Gilfedder, B. S., Weller, R. and Platt, U.: Iodine monoxide in the

459   Antarctic snowpack, Atmos. Chem. Phys., 10(5), 2439–2456 [online] Available from:

460   http://www.atmos-chem-phys.net/10/2439/2010/, 2010.

461   Gómez Martín, J. C., Spietz, P. and Burrows, J. P.: Spectroscopic studies of the I-2/O-3

462   photochemistry - Part 1: Determination of the absolute absorption cross sections of iodine oxides

463   of atmospheric relevance, J. Photochem. Photobiol. A - Chem., 176(1–3), 15–38,

464   doi:10.1016/j.jphotochem.2005.09.024, 2005.

465   Grilli, R., Legrand, M., Kukui, A., Méjean, G., Preunkert, S. and Romanini, D.: First

466   investigations of IO, BrO, and NO2 summer atmospheric levels at a coastal East Antarctic site

467   using mode-locked cavity enhanced absorption spectroscopy, Geophys. Res. Lett., 40(4), 791–

468   796, doi:10.1002/grl.50154, 2013.

469   Hay, T.: MAX – DOAS measurements of bromine explosion events in McMurdo Sound ,

470   Antarctica, University of Canterbury., 2010.

471   Hollwedel, J., Wenig, M., Beirle, S., Kraus, S., Kühl, S., Wilms-Grabe, W., Platt, U. and

472   Wagner, T.: Year-to- Year Variability of Polar Tropospheric BrO as seen by GOME, Adv. Sp.

473   Res., 34, 804–808 [online] Available from: http://dx.doi.org/10.1016/j.asr.2003.08.060, 2004.

474   Hönninger, G., von Friedeburg, C. and Platt, U.: Multi axis differential optical absorption

475   spectroscopy (MAX-DOAS), Atmos. Chem. Phys., 4, 231–254, doi:10.5194/acp-4-231-2004,

476   2004.

477   Inamdar, S., Tinel, L., Chance, R., Carpenter, L. J., Sabu, P., Chacko, R., Tripathy, S. C., Kerkar,

478   A. U., Sinha, A. K., Bhaskar, P. V., Sarkar, A., Roy, R., Sherwen, T., Cuevas, C., Saiz-Lopez,

Atmospheric
Chemistry
and Physics
Discussions

479   A., Ram, K., Mahajan, A. S., Pintér, Á. and De Weger, B. M. M.: Estimation of Reactive

480   Inorganic Iodine Fluxes in the Indian and Southern Ocean Marine Boundary Layer, Atmos.

481   Chem. Phys. Discuss., doi:10.5194/acp-2019-1052, 2020.

482   Jin, Z., Charlock, T. P., Smith, W. L. and Rutledge, K.: A parameterization of ocean surface

483   albedo, Geophys. Res. Lett., 31(22), 1–4, doi:10.1029/2004GL021180, 2004.

484   Koenig, T. K., Baidar, S., Campuzano-Jost, P., Cuevas, C. A., Dix, B., Fernandez, R. P., Guo,

485   H., Hall, S. R., Kinnison, D., Nault, B. A., Ullmann, K., Jimenez, J. L., Saiz-Lopez, A. and

486   Volkamer, R.: Quantitative detection of iodine in the stratosphere, Proc. Natl. Acad. Sci., (15),

487   201916828, doi:10.1073/pnas.1916828117, 2020.

488   Kreher, K., Johnston, P. V., Wood, S. W., Nardi, B. and Platt, U.: Ground-based measurements

489   of tropospheric and stratospheric BrO at Arrival Heights, Antarctica, Geophys. Res. Lett.,

490   24(23), 3021–3024, doi:10.1029/97GL02997, 1997.

491   Legrand, M., McConnell, J. R., Preunkert, S., Arienzo, M., Chellman, N., Gleason, K., Sherwen,

492   T., Evans, M. J. and Carpenter, L. J.: Alpine ice evidence of a three-fold increase in atmospheric

493   iodine deposition since 1950 in Europe due to increasing oceanic emissions, Proc. Natl. Acad.

494   Sci., 115(48), 12136–12141, doi:10.1073/pnas.1809867115, 2018.

495   Lewis, T., Gómez Martin, J. C., Blitz, M., Cuevas, C., Plane, J. and Saiz-Lopez, A.:

496   Determination of the absorption cross-sections of higher order iodine oxides at 355 nm and 532

497   nm, Atmos. Chem. Phys. Discuss., 1–28, doi:10.5194/acp-2020-456, 2020.

498   Mahajan, A. S., Shaw, M., Oetjen, H., Hornsby, K. E., Carpenter, L. J., Kaleschke, L., Tian-

499   Kunze, X., Lee, J. D., Moller, S. J., Edwards, P. M., Commane, R., Ingham, T., Heard, D. E. and

500   Plane, J. M. C.: Evidence of reactive iodine chemistry in the Arctic boundary layer, J. Geophys.

501   Res., 115(D20303,), doi:dx.doi.org/10.1029/2009JD013665, 2010.

502   Mahajan, A. S., Gómez Martín, J. C., Hay, T. D., Royer, S.-J., Yvon-Lewis, S. A., Liu, Y., Hu,

503   L., Prados-Román, C., Ordóñez, C., Plane, J. M. C. and Saiz-Lopez, A.: Latitudinal distribution

504   of reactive iodine in the Eastern Pacific and its link to open ocean sources, Atmos. Chem. Phys.,

505   12, 11609–11617, doi:10.5194/acp-12-11609-2012, 2012.

506   Mahajan, A. S., Tinel, L., Hulswar, S., Cuevas, C. A., Wang, S., Ghude, S., Naik, R. K., Mishra,

507   R. K., Sabu, P., Sarkar, A., Anilkumar, N. and Saiz Lopez, A.: Observations of iodine oxide in

508   the Indian Ocean marine boundary layer: A transect from the tropics to the high latitudes, Atmos.

509   Environ. X, 1, 100016, doi:10.1016/j.aeaoa.2019.100016, 2019.

510   Meller, R. and Moortgat, G. K.: Temperature dependence of the absorption cross sections of

511   formaldehyde between 223 and 323 K in the wavelength range 225-375 nm, J. Geophys. Res.,

512   105(D6), 7089–7101 [online] Available from: http://dx.doi.org/10.1029/1999JD901074, 2000.

513   Perovich, D. K., Grenfell, T. C., Light, B. and Hobbs, P. V.: Seasonal evolution of the albedo of

514   multiyear Actic sea ice, J. Geophys. Res. C Ocean., 107(10), doi:10.1029/2000jc000438, 2002.

515   Platt, U. and Stutz, J.: Differential optical absorption spectroscopy: Principles and applications,

516   First Edit., Springer., 2008.

517   Prakash Chaubey, J., Krishna Moorthy, K., Suresh Babu, S. and S. Nair, V.: The optical and

518   physical properties of atmospheric aerosols over the Indian Antarctic stations during southern

519   hemispheric summer of the International Polar Year 2007ĝ€"2008, Ann. Geophys., 29(1), 109–

520   121, doi:10.5194/angeo-29-109-2011, 2011.

521   Richter, A., Wittrock, F., Ladstätter-Weißenmayer, A. and Burrows, J. P.: GOME measurements

522   of stratospheric and tropospheric BrO, Adv. Sp. Res., 29(11), 1667–1672, 2002.

523   Rothman, L. S., Gordon, I. E., Babikov, Y., Barbe, A., Chris Benner, D., Bernath, P. F., Birk,

524   M., Bizzocchi, L., Boudon, V., Brown, L. R., Campargue, A., Chance, K., Cohen, E. a., Coudert,

525   L. H., Devi, V. M., Drouin, B. J., Fayt, A., Flaud, J.-M., Gamache, R. R., Harrison, J. J.,

526   Hartmann, J.-M., Hill, C., Hodges, J. T., Jacquemart, D., Jolly, A., Lamouroux, J., Le Roy, R. J.,

527   Li, G., Long, D. a., Lyulin, O. M., Mackie, C. J., Massie, S. T., Mikhailenko, S., Müller, H. S. P.,

528   Naumenko, O. V., Nikitin, A. V., Orphal, J., Perevalov, V., Perrin, A., Polovtseva, E. R.,

529   Richard, C., Smith, M. a. H., Starikova, E., Sung, K., Tashkun, S., Tennyson, J., Toon, G. C.,

530   Tyuterev, V. G. and Wagner, G.: The HITRAN 2012 molecular spectroscopic database, J. Quant.

531   Spectrosc. Radiat. Transf., 130, 4–50, doi:10.1016/j.jqsrt.2013.07.002, 2013.

532   Saiz-Lopez, A. and Blaszczak-boxe, C. S.: The polar iodine paradox, Atmos. Environ., 145, 72–

533   73, doi:10.1016/j.atmosenv.2016.09.019, 2016.

534   Saiz-Lopez, A. and von Glasow, R.: Reactive halogen chemistry in the troposphere., Chem. Soc.

535   Rev., doi:10.1039/c2cs35208g, 2012.

536   Saiz-Lopez, A., Mahajan, A. S., Salmon, R. A., Bauguitte, S. J.-B., Jones, A. E., Roscoe, H. K.

537   and Plane, J. M. C.: Boundary Layer Halogens in Coastal Antarctica, Science (80-.)., 317(5836),

538   348–351, doi:10.1126/science.1141408, 2007a.

539   Saiz-Lopez, A., Chance, K. V., Liu, X., Kurosu, T. P. and Sander, S. P.: First observations of

540   iodine oxide from space, Geophys. Res. Lett., 34(12), L12812, doi:10.1029/2007GL030111,

541   2007b.

542   Saiz-Lopez, A., Plane, J. M. C., Mahajan, A. S., Anderson, P. S., Bauguitte, S. J.-B., Jones, A.

543   E., Roscoe, H. K., Salmon, R. A., Bloss, W. J., Lee, J. D. and Heard, D. E.: On the vertical

544   distribution of boundary layer halogens over coastal Antarctica: implications for O-3, HOx, NOx

545   and the Hg lifetime, Atmos. Chem. Phys., 8(4), 887–900, 2008.

546   Saiz-Lopez, A., Plane, J. M. C., Baker, A. R., Carpenter, L. J., von Glasow, R., Martín, J. C. G.,

547   McFiggans, G. B., Saunders, R. W. and Gómez Martín, J. C.: Atmospheric Chemistry of Iodine,

548   Chem. Rev., 112(3), 1773–1804, doi:10.1021/cr200029u, 2012.

549   Saiz-Lopez, A., Blaszczak-Boxe, C. S. and Carpenter, L. J.: A mechanism for biologically-

550   induced iodine emissions from sea-ice, Atmos. Chem. Phys., 15, 9731–9746, doi::10.5194/acp-

551   15-9731-2015, 2015a.

552   Saiz-Lopez, A., Baidar, S., Cuevas, C. A., Koenig, T. K., Fernandez, R. P., Dix, B., Kinnison, D.

553   E., Lamarque, J., Rodriguez-Lloveras, X., Campos, T. L. and Volkamer, R.: Injection of iodine

554   to the stratosphere, Geophys. Res. Lett., 42, 6852–6859, doi:10.1002/2015GL064796, 2015b.

555   Schönhardt, A., Richter, A., Wittrock, F., Kirk, H., Oetjen, H., Roscoe, H. K. and Burrows, J. P.:

556   Observations of iodine monoxide (IO) columns from satellite, Atmos. Chem. Phys., 8, 637–653

557   [online] Available from: http://hal-insu.archives-ouvertes.fr/hal-00296438/ (Accessed 30 April

558   2012), 2008.

559   Schönhardt, A., Begoin, M., Richter, a., Wittrock, F., Kaleschke, L., Gómez Martín, J. C. and

560   Burrows, J. P.: Simultaneous satellite observations of IO and BrO over Antarctica, Atmos.

561   Chem. Phys., 12(14), 6565–6580, doi:10.5194/acp-12-6565-2012, 2012.

562   Stutz, J., Kim, E. S., Platt, U., Bruno, P., Perrino, C. and Febo, A.: UV-visible absorption cross

563   sections of nitrous acid, J. Geophys. Res., 105(D11), 14585–14592, 2000.

564   Thalman, R. and Volkamer, R. A.: Temperature Dependent Absorption Cross-Sections of O2-O2

565   collision pairs between 340 and 630 nm and at atmospherically relevant pressure, Phys. Chem.

566   Chem. Phys., 15, 15371–15381, doi:10.1039/C3CP50968K, 2013.

567   Theys, N., Van Roozendael, M., Hendrick, F., Yang, X., De Smedt, I., Richter, A., Begoin, M.,

568   Errera, Q., Johnston, P. V., Kreher, K. and De Mazière, M.: Global observations of tropospheric

569   BrO columns using GOME-2 satellite data, Atmos. Chem. Phys., 11, 1791–1811,

570   doi:10.5194/acp-11-1791-2011, 2011.

571   Vallelonga, P., Maffezzoli, N., Moy, A. D., Curran, M. A. J., Vance, T. R., Edwards, R., Hughes,

572   G., Barker, E., Spreen, G., Saiz-Lopez, A., Corella, J. P., Cuevas, C. A. and Spolaor, A.: Sea-ice-

573   related halogen enrichment at Law Dome, coastal East Antarctica, Clim. Past, 13(2), 171–184,

574   doi:10.5194/cp-13-171-2017, 2017.

575   Vandaele, A. C., Hermans, C., Simon, P., Carleer, M. R., Colins, R., Fally, F., Merienne, M. F.,

576   Jenouvrier, A. and Coquart, B.: Measurements of NO2 absorption cross-sections at 42000 cm-1

577   to 10000 cm-1 (238-1000 nm) at 220 K and 298 K, J. Quant. Spectrosc. Radiat. Transf., 59, 171–

578   184, 1997.

579   Vandaele, A. C., Hermans, C., Simon, P. C., Carleer, M., Colin, R., Fally, S., Merienne, M. F.,

580   Jenouvrier, A. and Coquartii, B.: Measurements od the NO2 absorption cross-section from 42000

581   cm-1 to 10000 cm-1 (238-1000 nm) at 220 K and 294 K, J. Quant. Spectrosc. Radiat. Transf.,

582   59(3), 171–184, 1998.

583   Wagner, T., Leue, C., Wenig, M., Pfeilsticker, K. and Platt, U.: Spatial and temporal distribution

584   of enhanced boundary layer BrO concentrations measured by the GOME instrument aboard

585   ERS-2, J. Geophys. Res. - Atmos., 106(D20), 24225–24235, 2001.

586   Wagner, T., Dix, B., Friedeburg, C. V., Frieß, U., Sanghavi, S., Sinreich, R. and Platt, U.: MAX-

587   DOAS O 4 measurements: A new technique to derive information on atmospheric aerosols—

588   Principles and information content, J. Geophys. Res., 109(D22), doi:10.1029/2004JD004904,

589   2004.

590   Wagner, T., Beirle, S. and Deutschmann, T.: Three-dimensional simulation of the Ring effect in

591   observations of scattered sun light using Monte Carlo radiative transfer models, Atmos. Meas.

592   Tech., 2(1), 113–124, doi:10.5194/amt-2-113-2009, 2009.

593   Wagner, T., Apituley, A., Beirle, S., Dörner, S., Friess, U., Remmers, J. and Shaiganfar, R.:

594   Cloud detection and classification based on MAX-DOAS observations, Atmos. Meas. Tech.,

595   7(5), 1289–1320, doi:10.5194/amt-7-1289-2014, 2014.

596   Wagner, T., Beirle, S., Benavent, N., Bösch, T., Chan, K. L., Donner, S., Dörner, S., Fayt, C.,

597   Frieß, U., García-Nieto, D., Gielen, C., González-Bartolome, D., Gomez, L., Hendrick, F.,

598   Henzing, B., Jin, J. L., Lampel, J., Ma, J., Mies, K., Navarro, M., Peters, E., Pinardi, G.,

599   Puentedura, O., Puķīte, J., Remmers, J., Richter, A., Saiz-Lopez, A., Shaiganfar, R., Sihler, H.,

600   Van Roozendael, M., Wang, Y. and Yela, M.: Is a scaling factor required to obtain closure

601   between measured and modelled atmospheric O&lt;sub&gt;4&lt;/sub&gt;

602   absorptions? An assessment of uncertainties of measurements and radiative transfer simulations

603   for 2 selected days during th, Atmos. Meas. Tech., 12(5), 2745–2817, doi:10.5194/amt-12-2745-

604   2019, 2019.

605

607   Figures
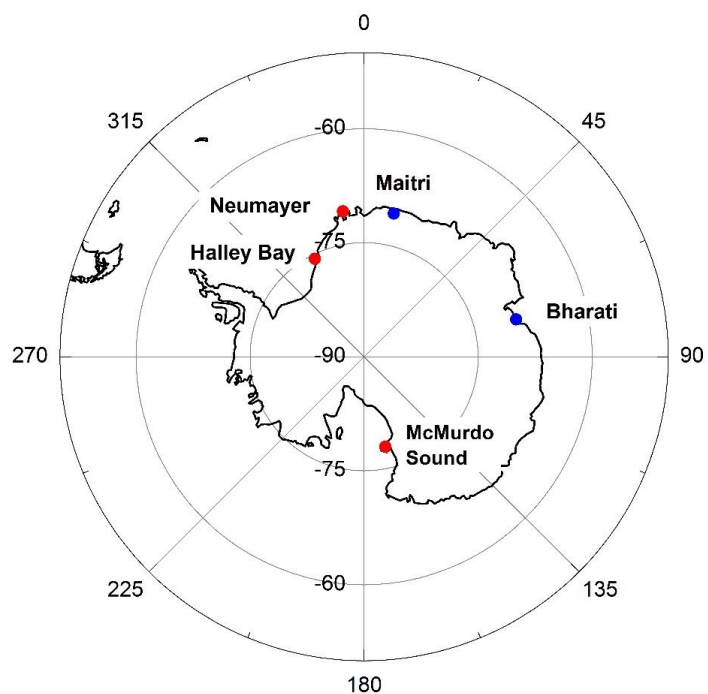
608

609   **Figure 1:** Map showing the location of the two Indian Antarctic stations, Maitri and Bharati, where

610   observations of IO were performed during this study (blue dots). Previous locations that have

611   reported observations of IO are also marked on the map (red dots).

612
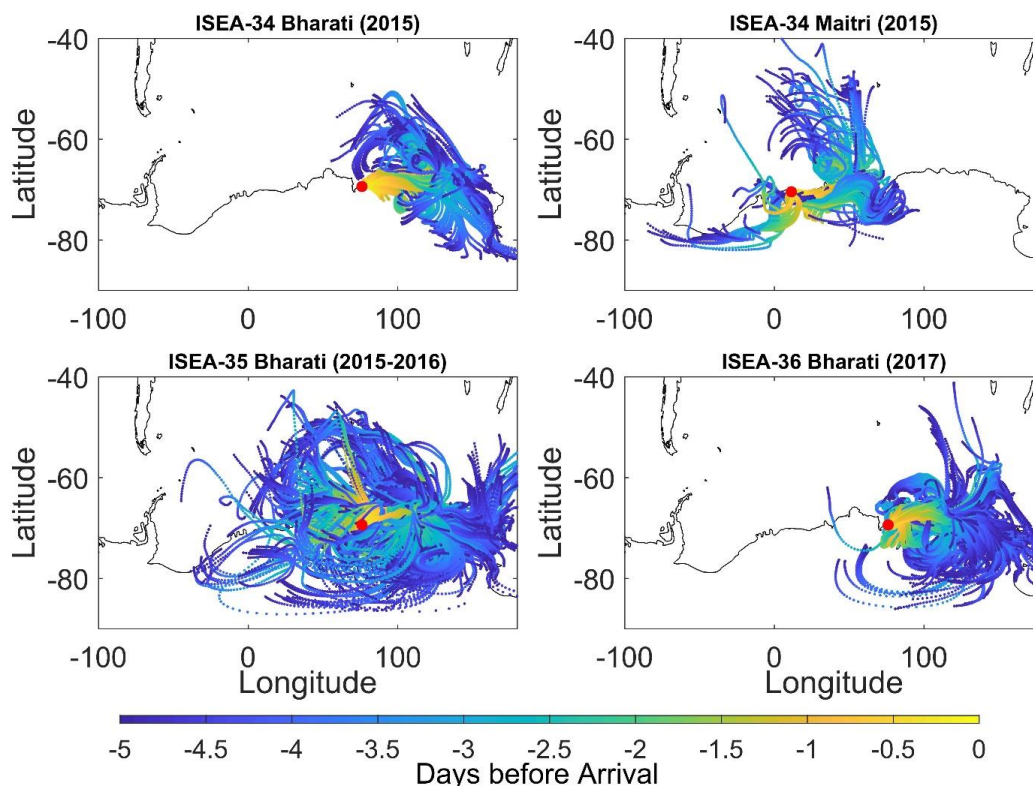
Figure 2: 5-day back-trajectories arriving at the two stations on the days that the measurements of IO were conducted as a part of the 34th, 35th and 36th ISEA expeditions are shown. The back-trajectories were calculated using the HYbrid Single-Particle Lagrangian Integrated Trajectory (HYSPLIT) model, arriving every hour (Draxler and Rolph, 2003).
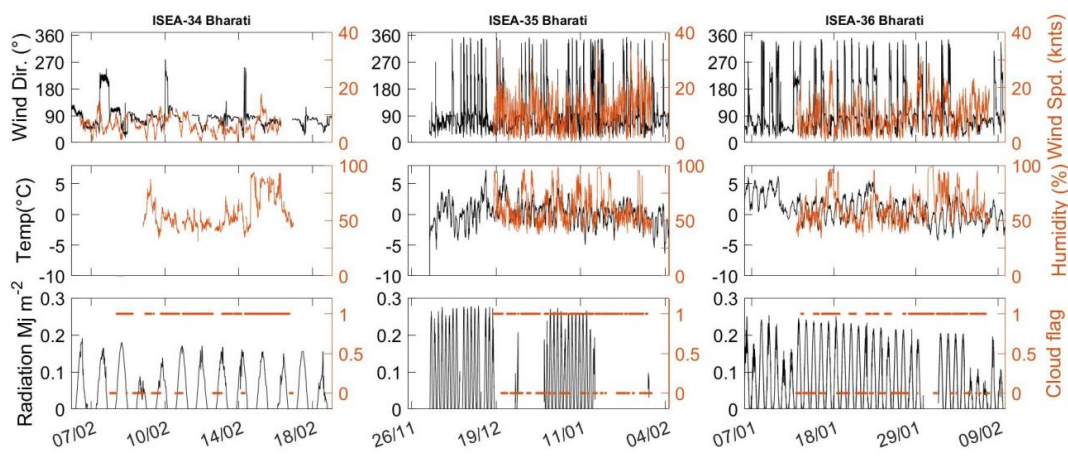
Figure 3: Observations of different meteorological parameters that were measured during the various summer campaigns are shown here. The top panels show the wind direction and speed; the middle panels show the temperature and humidity; and the bottom panels show the radiation and cloudiness (1 is defined as 30% cloudy skies and above). Observations of these parameters were not made during the 34th ISEA at Maitri and the gaps indicate instrumental or observational issues.
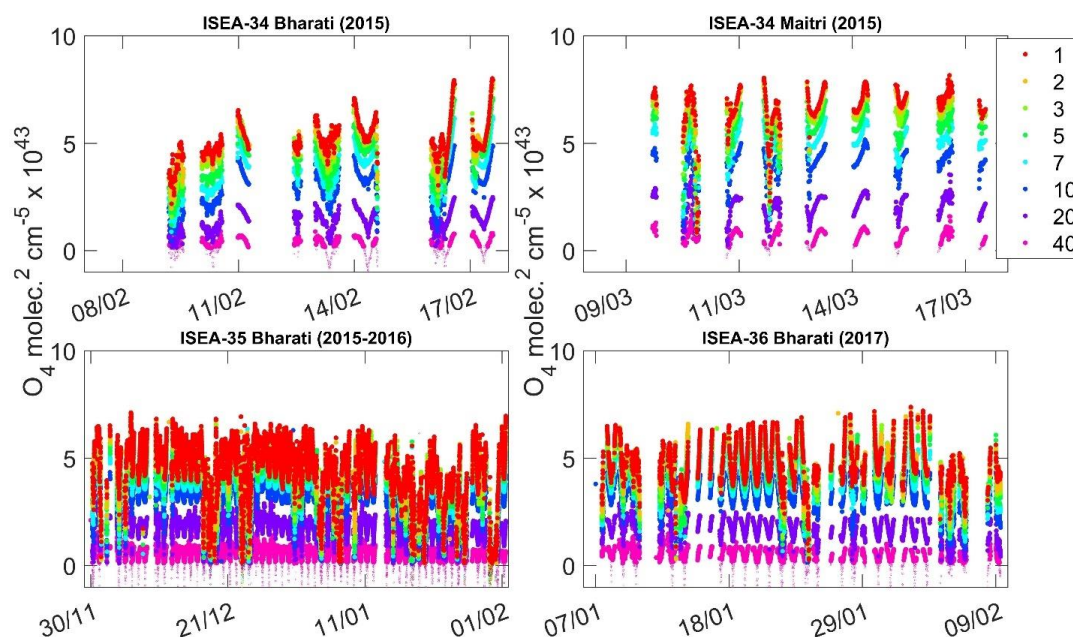
Figure 4: O_4 DSCDs observed during the four campaigns are shown. The empty circles represent values below the 2σ detection limit of the instrument, while the filled circles are values above the 2σ detection limit. The data are color-coded according to elevation angles.
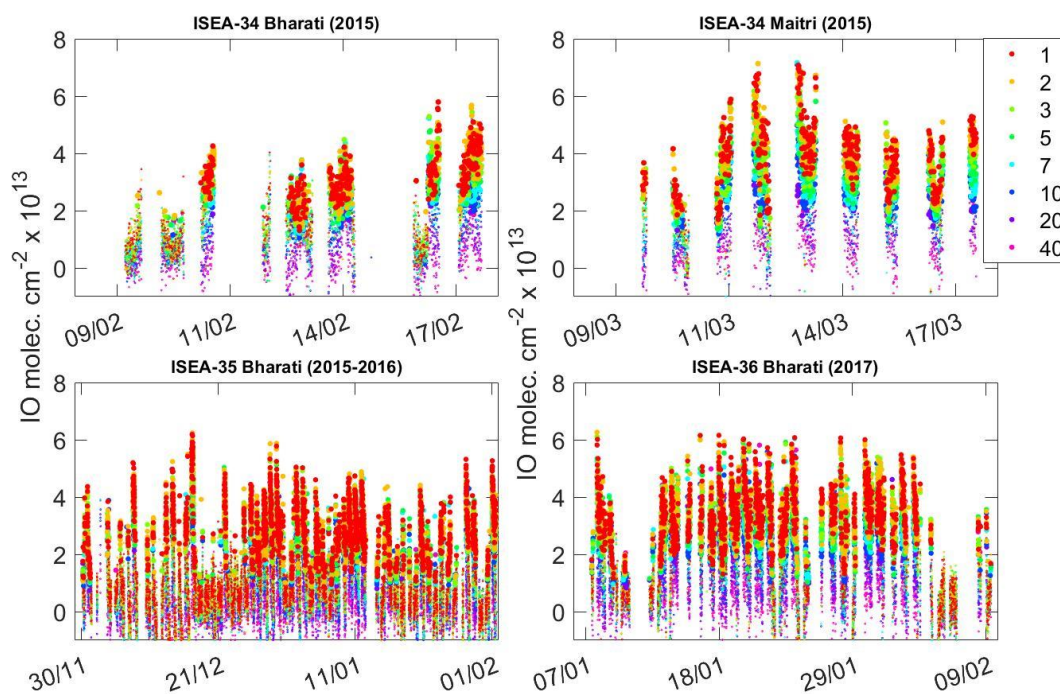
Figure 5: IO DSCDs observed during the four campaigns are shown. The smaller circles represent values below the 2σ detection limit of the instrument, while the bigger circles are values above the 2σ detection limit. The data are color-coded according to elevation angles.

636

637
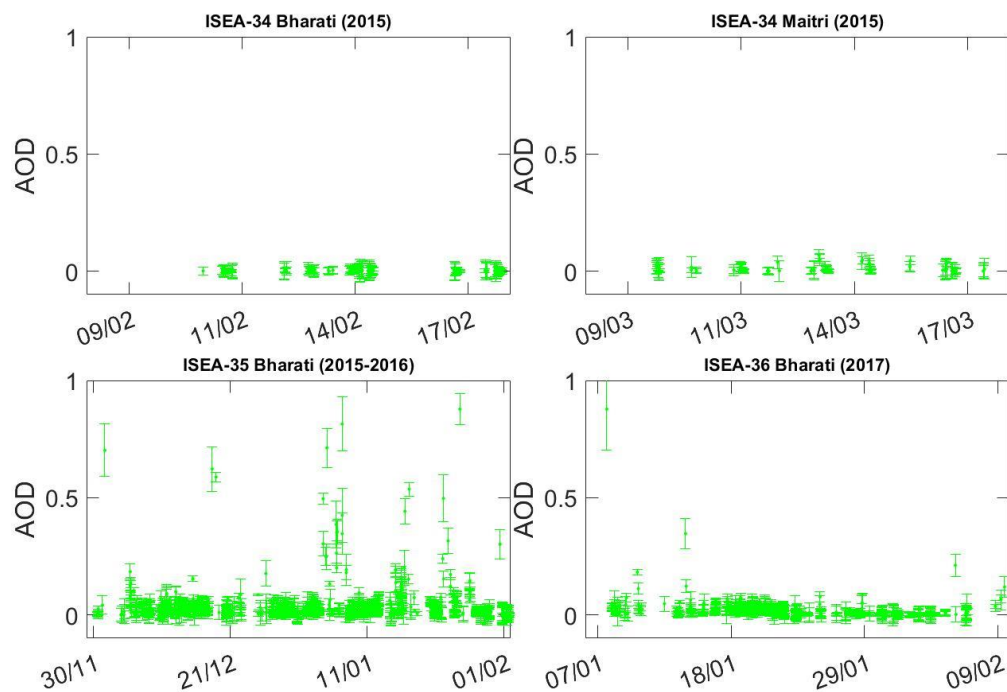
Figure 6: AOD timeseries retrieved using the O₄ DSCDs for all the four campaigns are shown.

The data show only the 'good' datapoints, which are reliable and were mostly during clear sky

conditions.

641

642
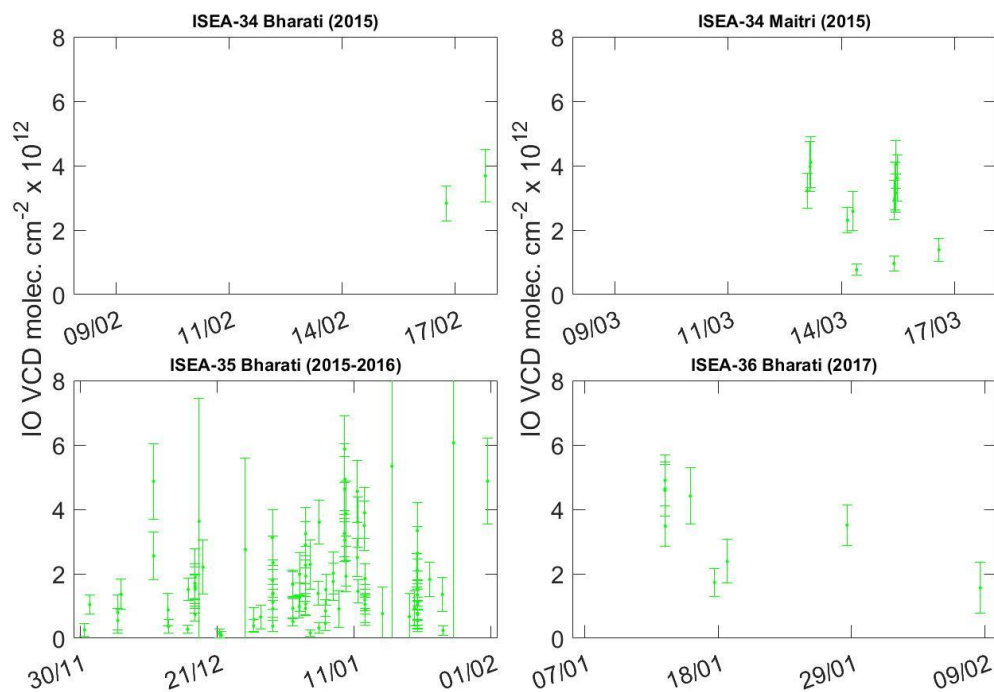
Figure 7: Observations of IO vertical column densities observed through all the four campaigns

are shown. These data were mostly during periods of clear sky, and where IO was observed above

the detection limit for most of the set elevation angles, enabling a reliable profile retrieval.

646
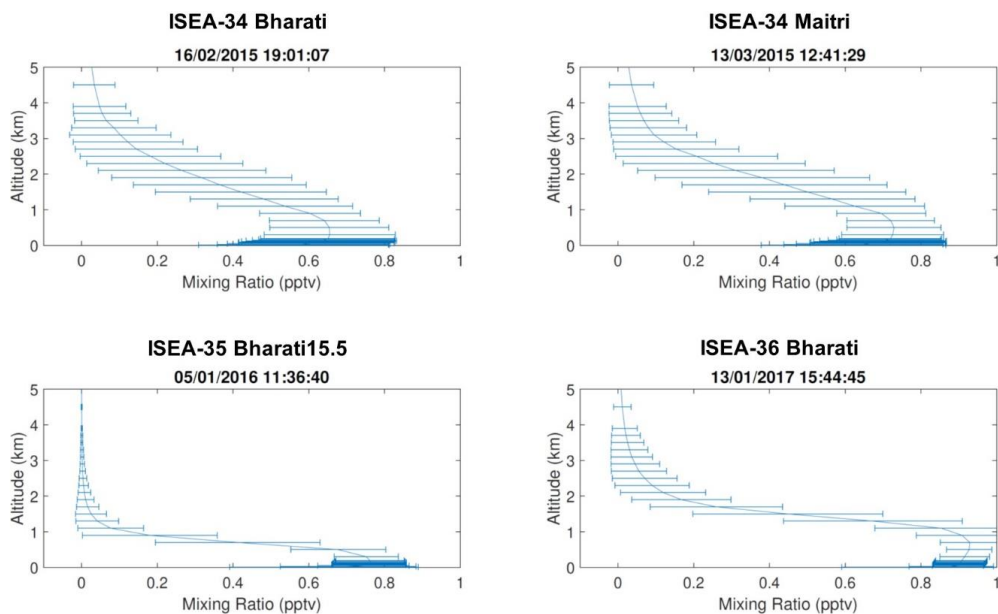
Figure 8: Typical examples of IO vertical profiles retrieved during all the four campaigns are
shown.

651
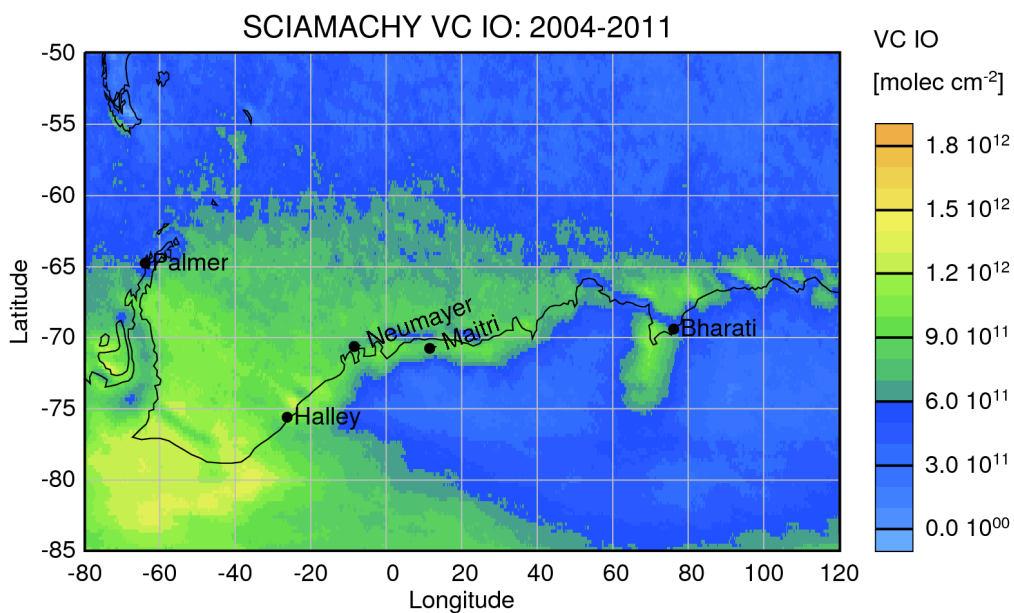
Figure 9: Averaged VCDs of IO as retrieved by SCIAMACHY between 2004-2011are shown.

Observations suggest that lower levels of IO are expected at Bharati and Maitri, as compared to

Halley Bay and Neumayer.

655

Atmospheric
Chemistry
and Physics
Discussions
Open Access
EGU

656
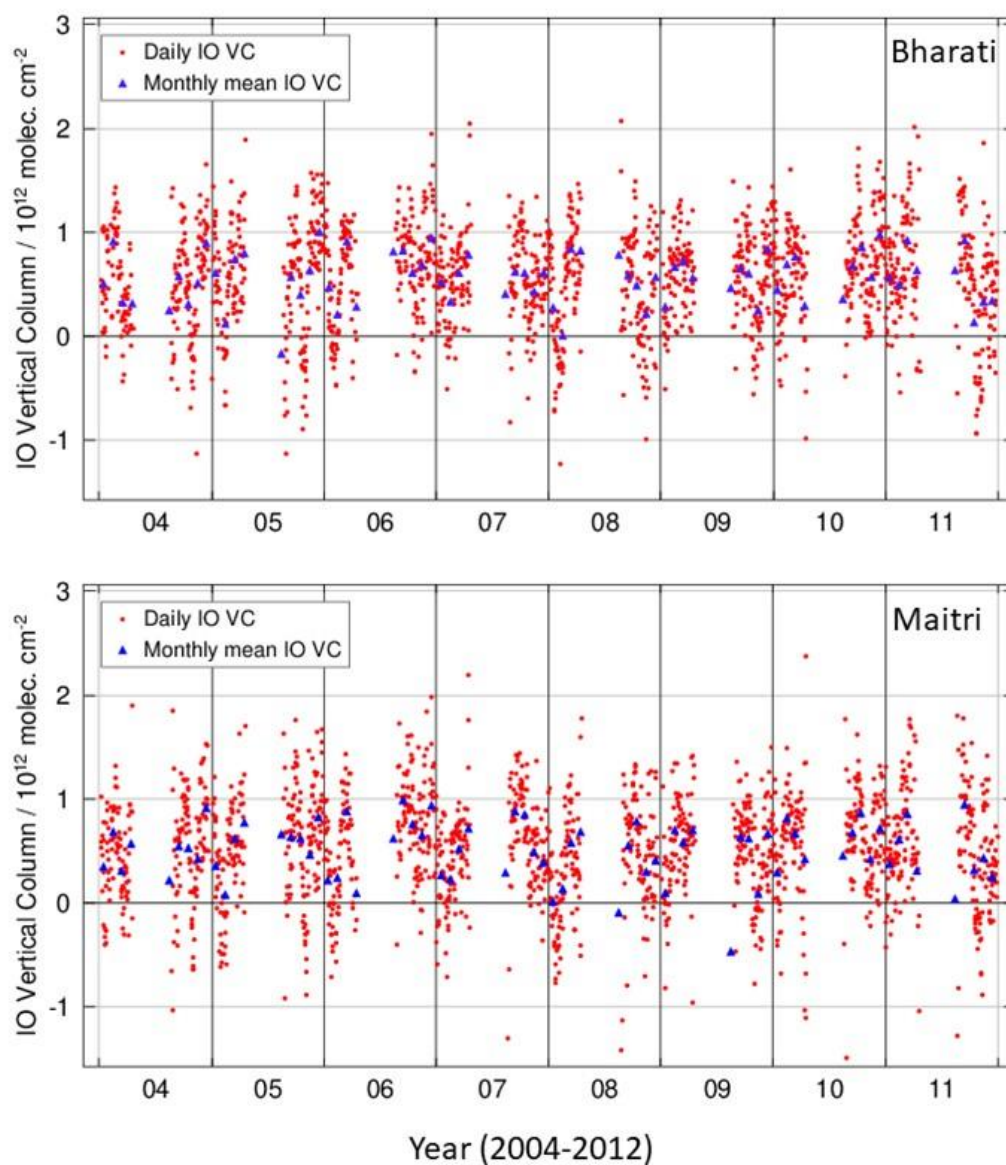
Figure 10: Timeseries of IO VCD observations at the Bharati station as retrieved by
SCIAMACHY. The monthly mean values are shown in blue, and the daily datapoints are shown
in red.